PNAS
www.pnas.org

Supplementary Information for

Reconfigurable multifunctional ferrofluid droplet robots

Xinjian Fan[a,b,1], Xiaoguang Dong[a,1], Alp C. Karacakol[a,c], Hui Xie[b], Metin Sitti[a,d] *

[a] Physical Intelligence Department, Max Planck Institute for Intelligent Systems, Stuttgart 70569, Germany

[b] State Key Laboratory of Robotics and Systems, Harbin Institute of Technology, Harbin 150080, China

[c] Department of Mechanical Engineering, Carnegie Mellon University, Pittsburgh, PA 15213, USA

[d] Institute for Biomedical Engineering, ETH Zurich, Zurich 8092, Switzerland

[1] Equally contributing first authors

* Correspondence to: sitti@is.mpg.de

The PDF file includes:

> Fig. S1 to Fig. S17.
> Table S1 to Table S2.
> Supplementary Text.
> Legends for Movies S1 to S6.
> SI References.

Other supplementary material for this manuscript includes the following:

> Movie S1. Mechanism and characterization of controlling large complex shapes of FDRs.
> Movie S2. Mechanism and characterization of controlling motions of FDRs.
> Movie S3. Mechanism and characterization of FDRs navigating in confined spaces.
> Movie S4. Efficient manipulation of delicate objects by shape-programmable FDRs.
> Movie S5. Cargo delivery in tubal environments towards biomedical applications.
> Movie S6. Multiple FDRs demonstrating programmable fluidic mixing by coordinated independent motion control.
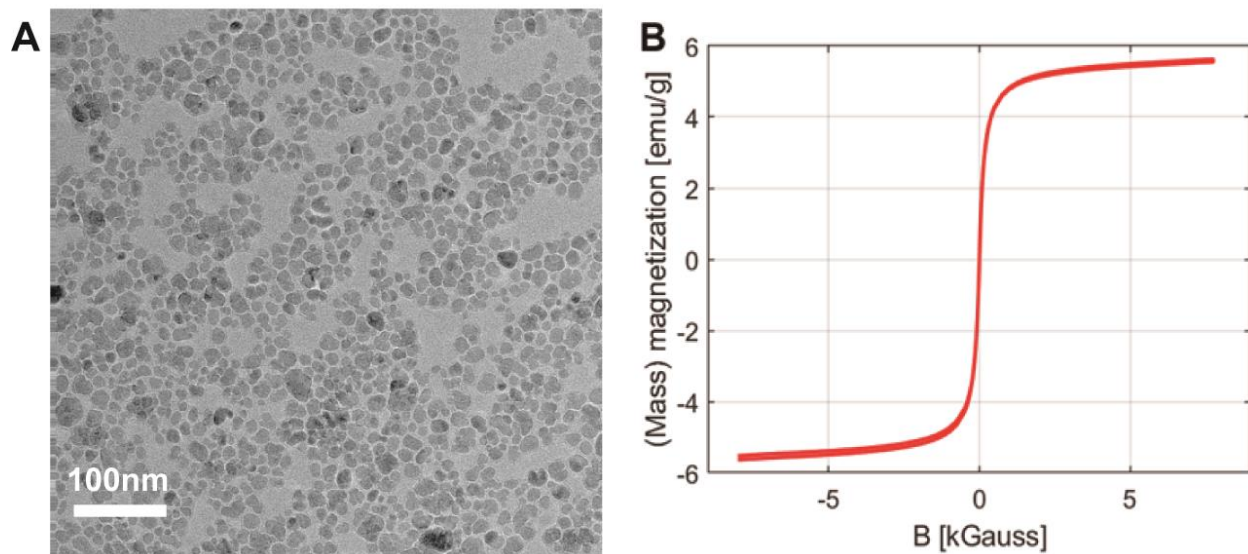
Supplementary Figures and Tables

Fig. S1. Transmission electron microscope (TEM) image and magnetization hysteresis curve of a ferrofluid droplet. (**A**) A Transmission Electron Microscope (TEM) image of the iron oxide nanocrystals in ferrofluids (MFR-DP1, Supermagnet.de). (**B**) The magnetization hysteresis curve of a ferrofluid droplet (55 μL). The measurements were carried out with a step size of 250 Oe/s in a vibrating sample magnetometer (EZ7 VSM, Microsense, LLC). The remanent magnetization (M_r) and coercivity (H_c) are both close to zero.
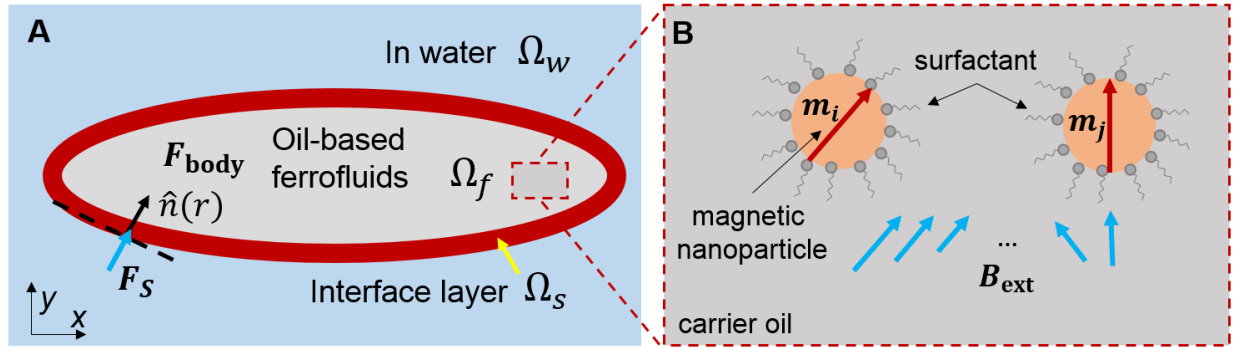
Fig. S2. Illustration of a continuum model of a ferrofluid droplet. (**A**) Two-dimensional (2D) schematics of the experienced forces by an FDR. The domains of the liquid outside, the ferrofluid, and the interface layer between the ferrofluid and the outside liquid are denoted as Ω_w, Ω_f and Ω_s, respectively. $\boldsymbol{F}_s$ and $\boldsymbol{F}_{\text{body}}$ represent the surface tension and other body forces applied on the droplet. (**B**) Illustration of the magnetizing process of a ferrofluid droplet subject to an external magnetic field $\boldsymbol{B}_{\text{ext}}(x, y, z, t)$ (blue arrows). m_i and m_j (red arrows) are the magnetic moments obtained by two magnetic nanoparticles.
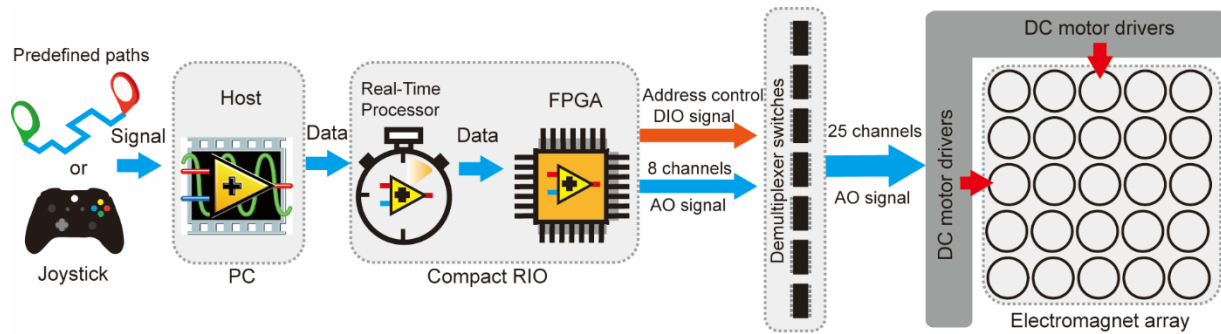
Fig. S3. Illustration of the electromagnet array actuation and control system. The electromagnet actuation and control system consists of 25 solenoids in a 5 × 5 array together with their power and control units. A lab PC is working as the host computer for the high-level human-computer interface and visualization of data. An embedded controller (Compact RIO, National Instruments, Inc.) is used as a low-level controller for real-time control of the DC motor drivers (Syren 25, Dimension Engineering). These motor drivers are powered by a DC power supply (N8951A, KeySight Inc.). Demultiplexers are used for utilizing eight analog output channels to control 25 DC motor drivers, by sending analog inputs to the selected DC motor drivers to actuate the coils at desired voltages.
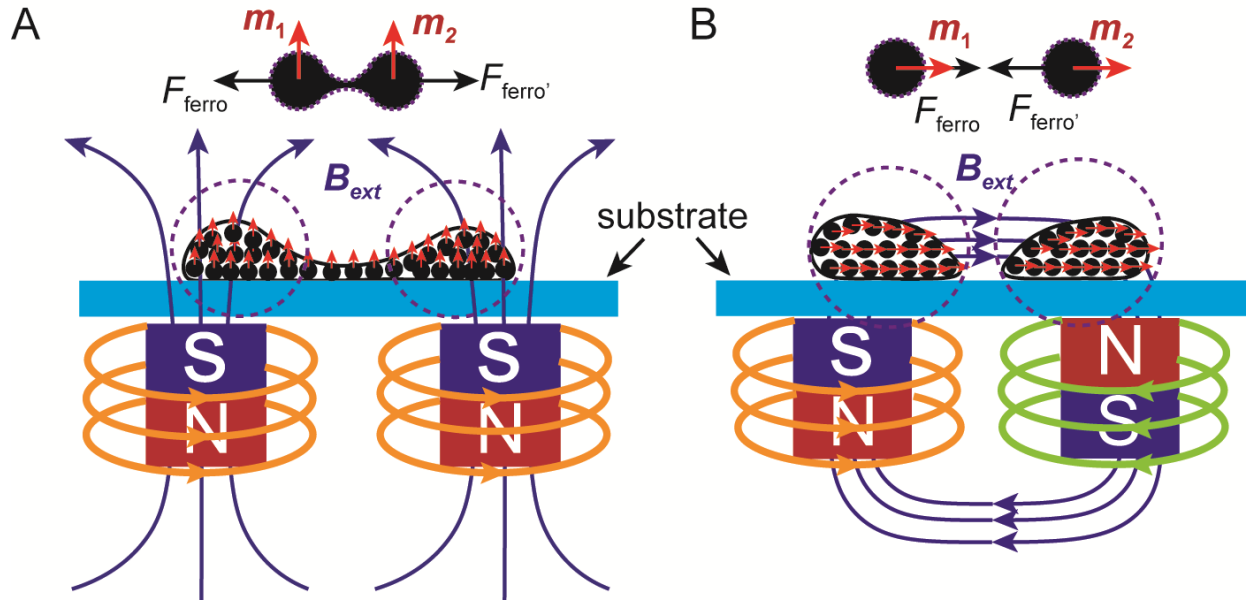
Fig. S4. Illustration of the effect of interactive magnetic forces in the splitting and merging process of FDRs. (**A**) Schematics of the magnetic interaction within an FDR in the splitting process. The magnetic particles have been magnetized along the direction of B_{ext}. Repulsive magnetic forces within an FDR help the splitting process under an external magnetic field B_{ext}. (**B**) Schematics of the magnetic interaction between two FDRs in the merging process. Attractive magnetic forces between two droplets contribute to the merging process of an FDR. In (**A**) and (**B**), F_{ferro} and $F_{ferro'}$ represent the interaction forces between two droplets. m_1 and m_2 (red arrows) are the net magnetic moments of droplets.
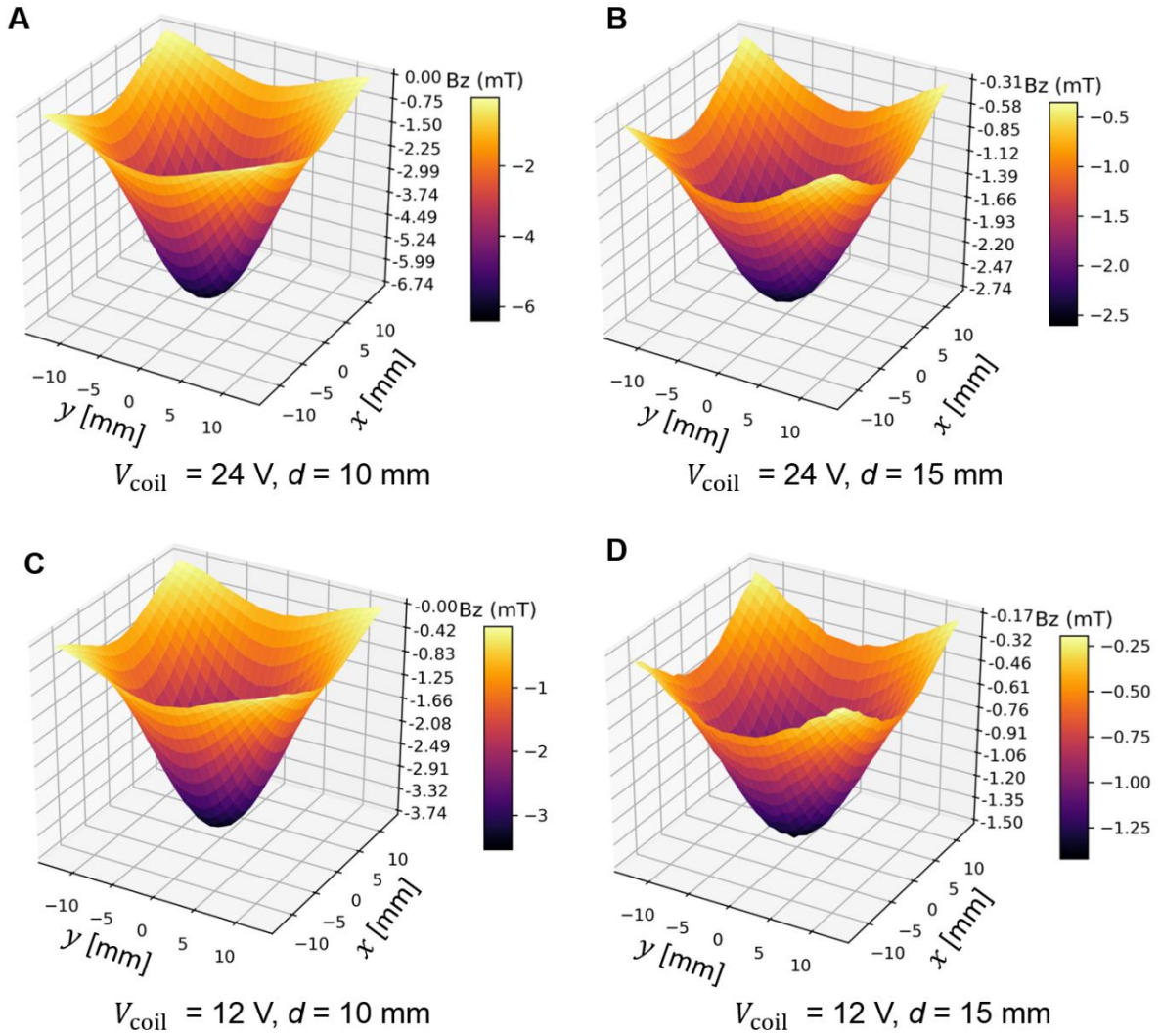
Fig. S5. Experimentally measured magnetic fields (B_z) as a function of the driving voltage and actuation distance in the electromagnet array system. (A) $V_{coil} = 24\,V$, $d = 10$ mm. (B) $V_{coil} = 24\,V$, $d = 15$ mm. (C) $V_{coil} = 12\,V$, $d = 10$ mm. (D) $V_{coil} = 12\,V$, $d = 15$ mm.
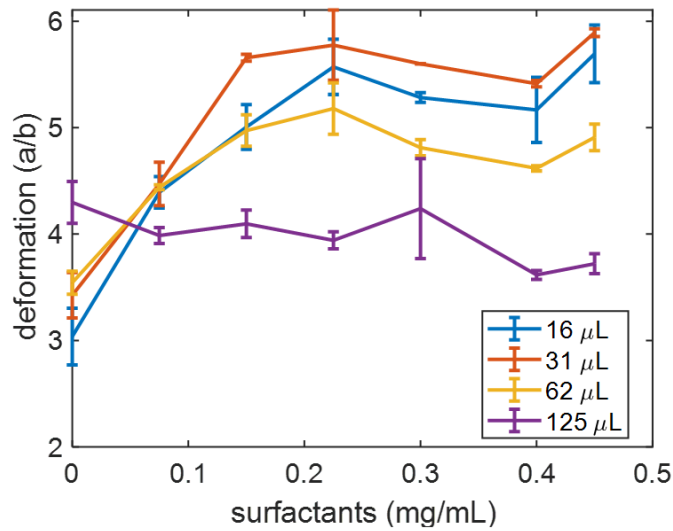
Fig. S6. Shape deformation of an FDR when varying its surface tension coefficient. The surface tension coefficient γ of the droplet is varied by mixing the surfactant sodium dodecyl sulfate (SDS) with water according to different mixing ratios. The FDR is actuated in the double-coil mode with a driving voltage of 15 V. When the volume of the FDR is less than 62 µL, its deformability is significantly affected by the surface tension coefficient. The error bars indicate standard deviations of $n = 5$ measurements in each trial.
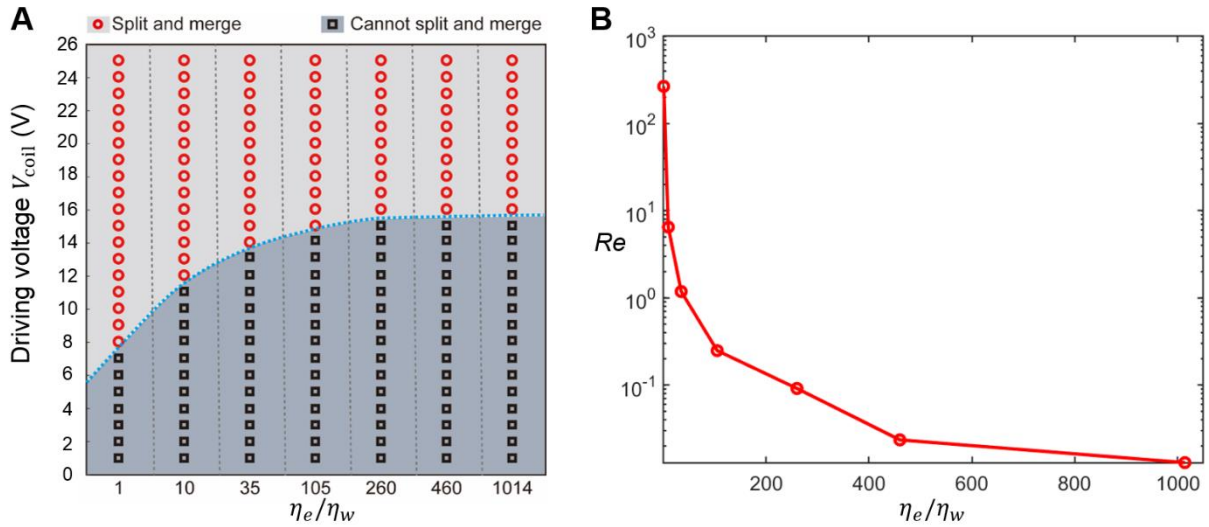
Fig. S7. **Analysis of the inertia effect in the splitting and merging behavior of an FDR.** (**A**) The minimal driving voltages to induce the splitting and merging behavior of an FDR in liquids of different dynamic viscosities. The FDR has a volume of about 210 μL and a dynamic viscosity of 8 mPa·s (EMG 901, Ferrotec Corporation). Liquids of different dynamic viscosities η_e are made from glycerol and water (dynamic viscosity: $\eta_w = 1$ mPa·s) with different mixing ratios. (**B**) Estimated Reynolds number (Re) of an FDR in the splitting process subject to a driving voltage of 15 V. Re is estimated using the average velocity of the FDR in the splitting process. In all figures, the x-axis represents the relative dynamic viscosity of the mixed liquid to that of water.
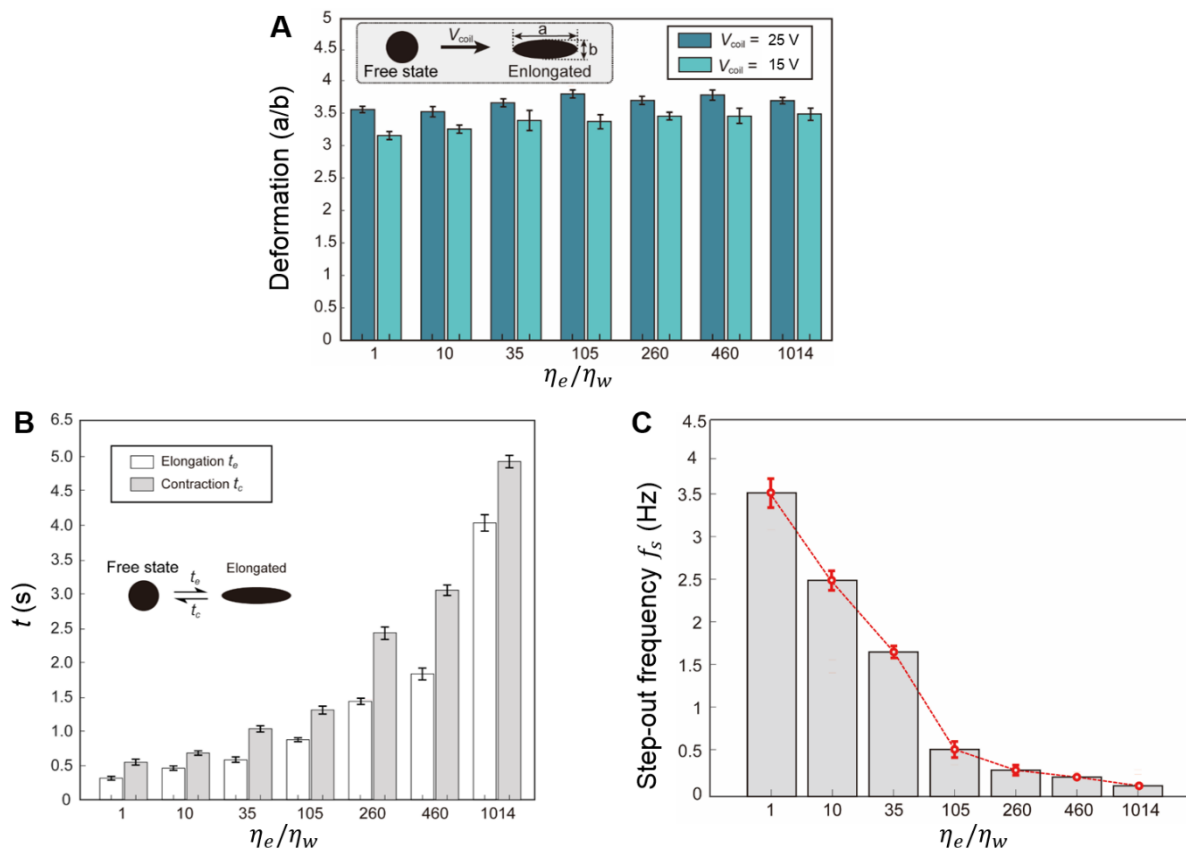
Fig. S8. Shape deformation and motion of an FDR in liquids of different viscosities. (**A**) Deformability of an FDR as a function of the dynamic viscosities of surrounding liquids. (**B**) Time of elongation and contraction of an FDR as a function of the dynamic viscosities of surrounding liquids. (**C**) Step-out frequency of the translational motion of an FDR as a function of the dynamic viscosities of surrounding liquids. The FDR has a volume of ~210 µL and a dynamic viscosity of 8 mPa·s (EMG 901, Ferrotec Corporation). In all figures, the *x*-axis represents the relative dynamic viscosity of the mixed liquid to that of water.
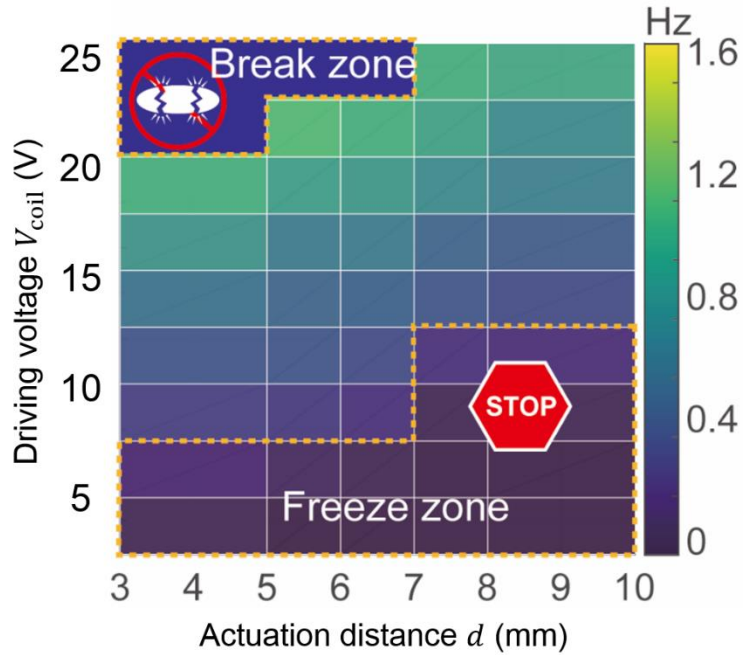
Fig. S9. Characterization of the step-out frequency for an FDR actuated in the single-coil mode in water. The step-out frequency is plotted as a function of the applied voltage V_{coil} (or the external magnetic field strength) and the actuation distance d from the top surface of the electromagnet array to the substrate surface.
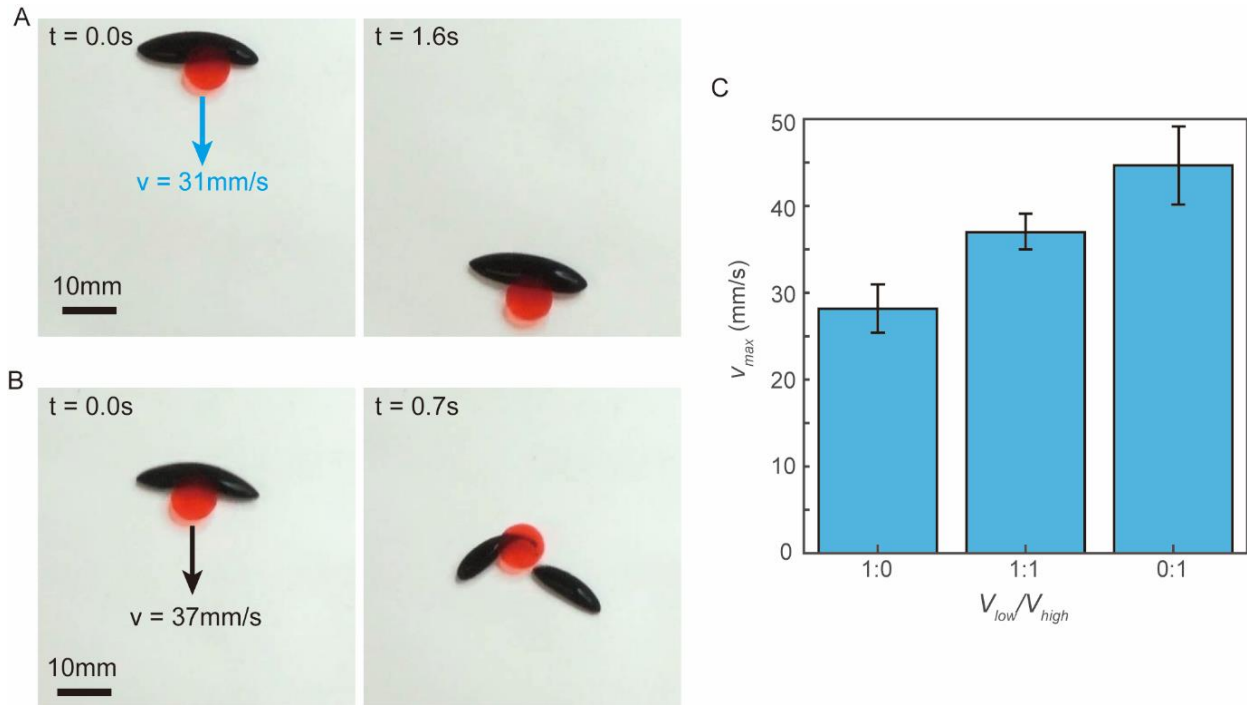
Fig. S10. Illustration of the safety mechanism of an FDR while manipulating delicate objects.
(**A**) Video snapshots of an FDR pushing an object without breaking. The FDR (MFR-DP1, Supermagnet.de) can push a hydrogel ball in a diameter of 11 mm while moving at a velocity of about 31 mm/s. (**B**) Video snapshots of an FDR pushing an object and ending up breaking into two parts. The FDR cannot push the hydrogel ball when the moving velocity is more than 37 mm/s. The FDR breaks into two parts due to the local resistance force from the hydrogel ball. The ferrofluids used in the experiment are obtained by mixing ferrofluids with dynamic viscosities of 80 mPa·s (MFR-DP1, Supermagnet.de) and 8 mPa·s (EMG 901, Ferrotec Corporation) according to a one-to-one volume ratio. (**C**) The maximal velocities of different ferrofluid droplets before breaking while pushing a hydrogel sphere as a function of the volume ratio of two ferrofluids (dynamic viscosities: $\eta_{low} = 8$ mPa $\cdot$ s , $\eta_{high} = 80$ mPa $\cdot$ s). In all experiments, the FDR and the object are submerged in the water in a glass petri dish.
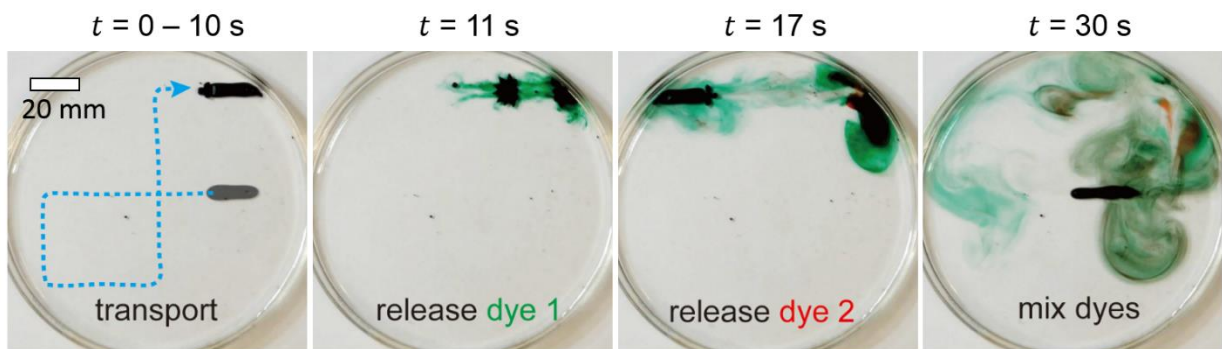
Fig. S11. Transportation of two types of dyes simultaneously by a single FDR. An FDR transports two types of liquid cargos (water-based food dyes) along a programmed trajectories ($t = $ 0 to 10 s). It first releases the dye in green color ($t = 11$ s), then releases the dye in red color ($t = $ 17 s), and finally mixes these two dyes ($t = 30$ s).
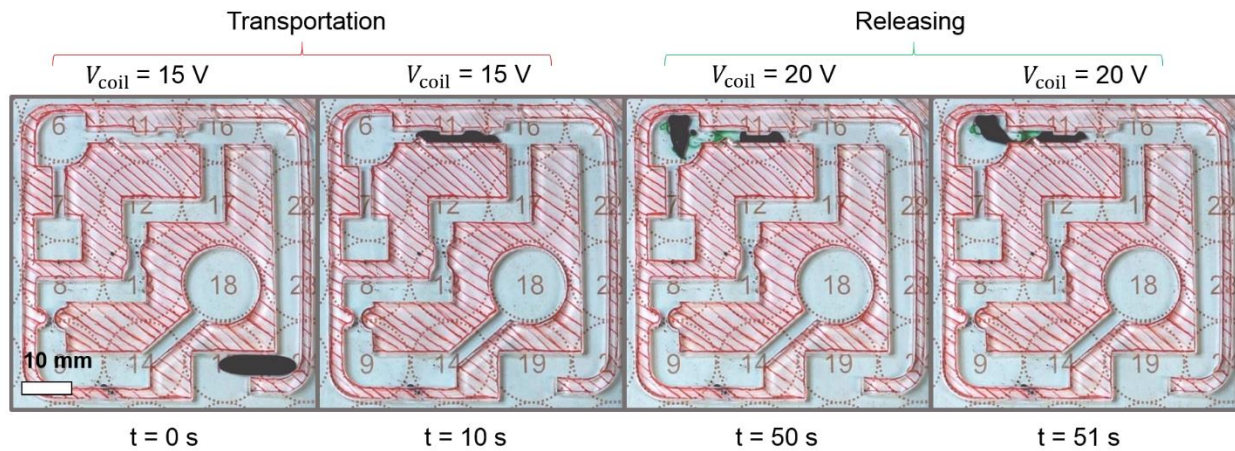
Fig. S12. Sequential video snapshots of transporting and releasing of liquid cargos by an FDR in a maze. A relatively small voltage (15 V) is used during the transportation process for safe transportation. A relatively large voltage (20 V) is used for efficiently splitting to release the cargo.
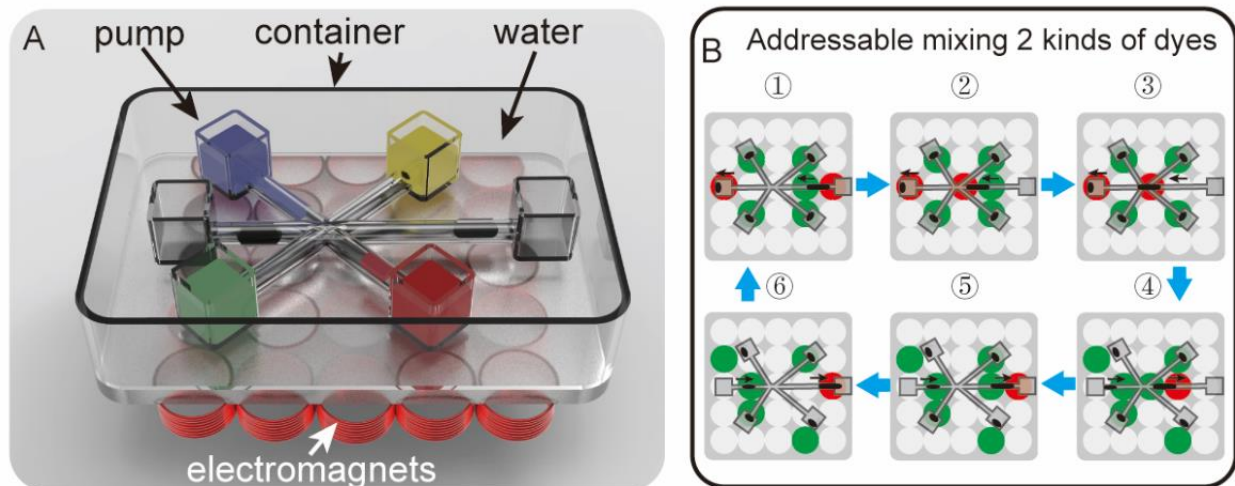
Fig. S13. Schematics and example control signals in the demonstration of selectively mixing two dyes. (**A**) Schematics of the fluidic channels and the electromagnet array. (**B**) The sequential control signals of the electromagnets when only mixing the blue and red dyes. The green and red circles indicate active coils with currents in the clockwise (CW) and counterclockwise (CCW) directions, respectively. The black arrows and blue arrows represent the motion of the pistons and the time sequence of the control signals respectively.
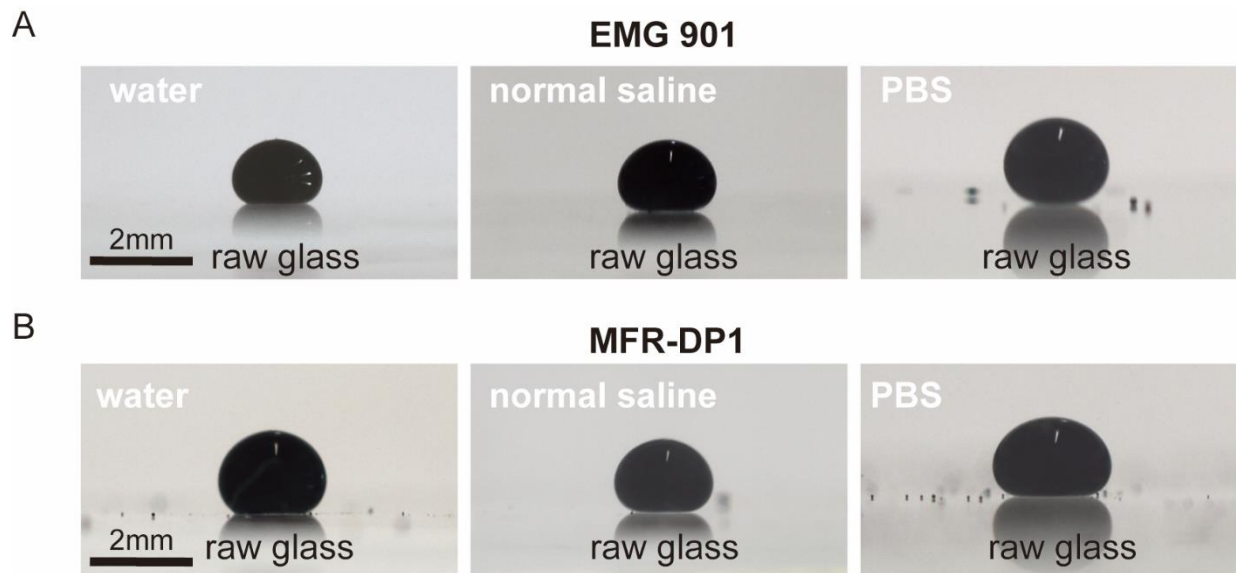
Fig. S14. Wettability of ferrofluid droplets in different water-based solutions. (**A**) Wettability of ferrofluid droplets (EMG 901, Ferrotec Corporation) in water, normal saline and phosphate-buffered saline (PBS) in a glass petri dish, respectively. (**B**) Wettability of ferrofluid droplets (MFR-DP1, Supermagnet.de) in water, normal saline and PBS in a glass petri dish, respectively.
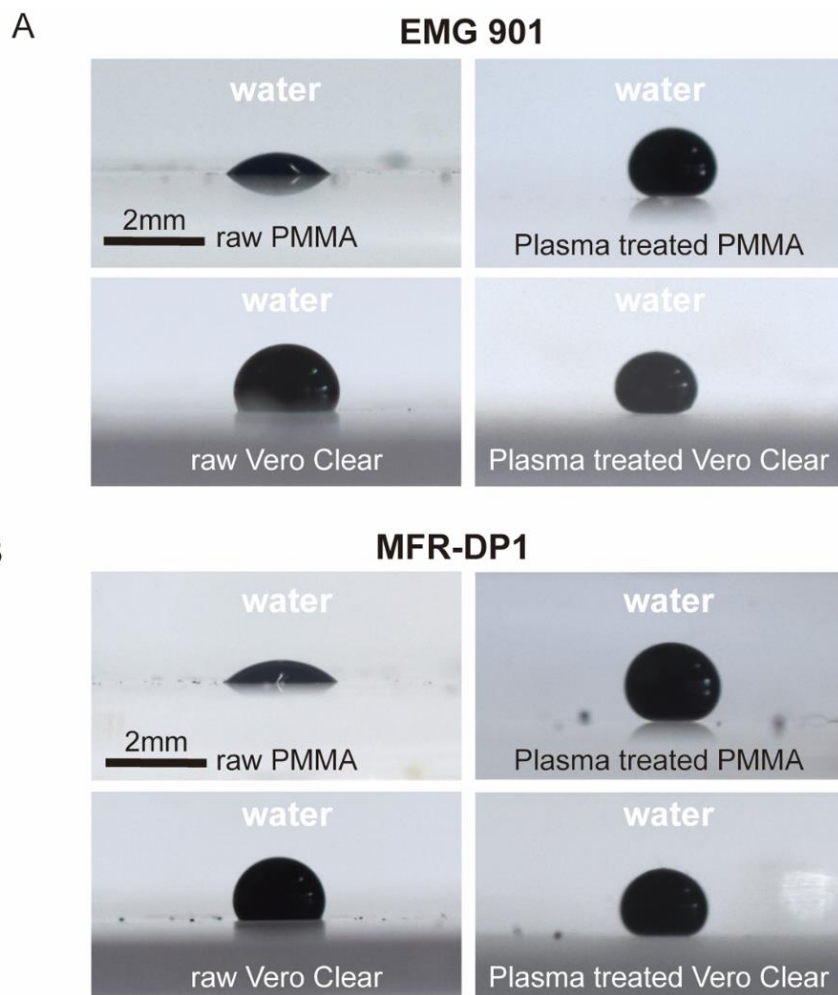
Fig. S15. Wettability of different ferrofluid droplets on various substrate surfaces in water. (**A**) Wettability of ferrofluid droplets (EMG 901, Ferrotec Corporation) on the surface of raw substrate surfaces (left) and plasma treated substrate surfaces (right). (**B**) Wettability of ferrofluid droplets (MFR-DP1, Supermagnet.de) on the surface of raw substrate surfaces (left) and plasma treated substrate surfaces (right), respectively.
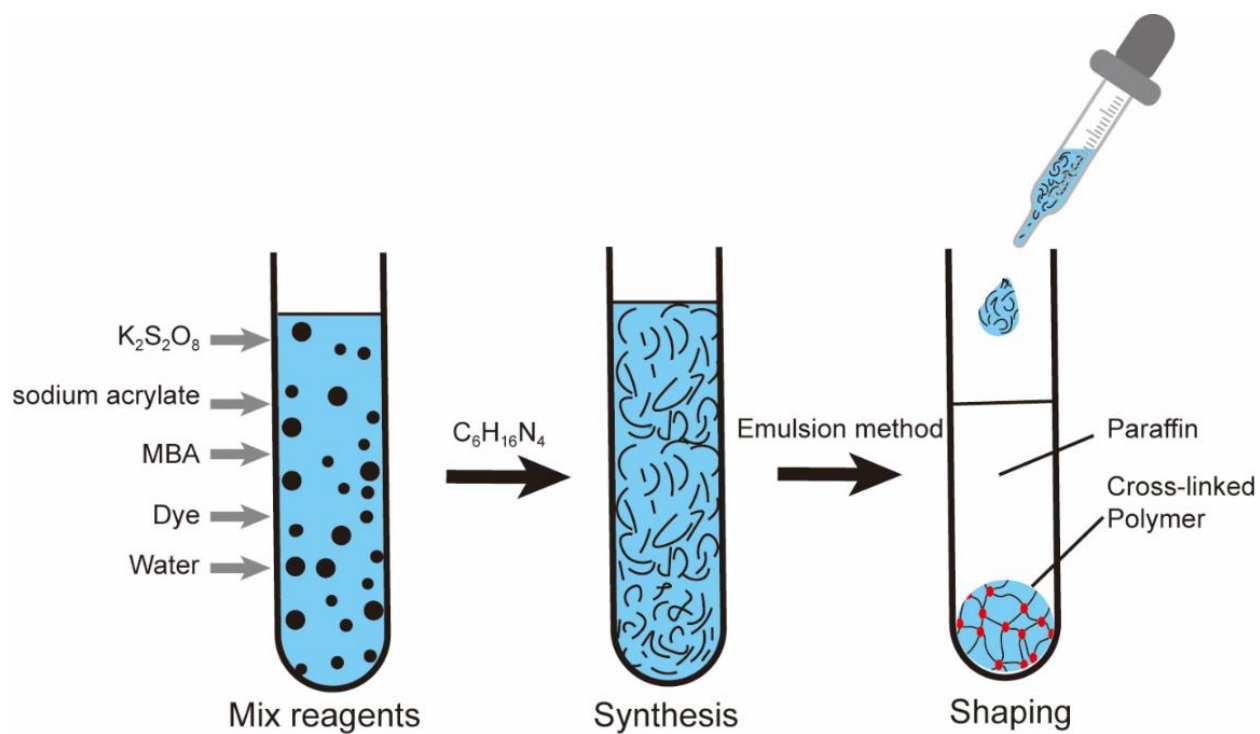
Fig. S16. Illustration of preparing spherical objects from a hydrogel. The polypodium acrylate hydrogel was synthesized by the free radical polymerization method. Firstly, sodium acrylate, N,N'-methylenebisacrylamide (MBA), and $K_2S_2O_8$ were dissolved in deionized water and ultrasonicated for 30 min. Then $C_6H_{16}N_4$ was then added into the solution before transferred to the tube with liquid paraffin contained for shaping.

Table S1. Properties of the ferrofluids used in the experiments.

Name	Density (g·cm⁻³)	Dynamic viscosity (mPa·s)	Magnetic Saturation (mT)	Carrier Liquid
EMG 901	1.43	8	66	Light Hydrocarbon Oil
MFR-DP1	1.04	80	30	Hydrocarbon Oil

Table S2. Parameters used in numerical simulations.

Parameter	Name	Value	Units
ρ_0	Ferrofluid density	1.43	$g \cdot cm^{-3}$
η	Ferrofluid dynamic viscosity	8	$mPa \cdot s$
μ_s	Friction coefficient	0.01	dimensionless
γ	Surface tension of the ferrolfuid in water	13.8	$mN \cdot m^{-1}$
χ	Volume magnetic susceptibility	0.54	dimensionless
K	Bulk modulus	1.2	GPa
λ	Incompressibility coefficient	7	dimensionless
m	Approximated magnetic moment of a solenoid	0.15	$A \cdot m^2$

** The external magnetic field is characterized and plotted in **Fig. S5**.

Supplementary Text

1. Preparation of tubular phantom structures and mazes

The vascular structure phantoms in **Fig. 4D** and **Fig. 6C** as well as the tubular structures in **Fig. 7D,E** were made of Vero Clear (Stratasys Inc.) printed by a 3D printer (Objet260 Connex3, Stratasys Inc.). The maze in **Fig. 4E** was manufactured by cutting Poly(methyl methacrylate) (PMMA) using a laser cutting machine (Mini 24, Epilog Laser Inc.). These structures were put into a plasma machine (Tergeo Plasma Cleaner, PIE Scientific LLC) for surface treatment for about 5 minutes to obtain hydrophilic surface properties. Then, the processed phantom structures were put into a glass petri dish filled with water. These surface treatments are desired as oil-based ferrofluid droplets would not wet on the treated hydrophilic substrate surface, as shown **Fig. S15**. This is because the water molecules assembled on the hydrophilic substrate surface form a thin film between the droplet and the surface, effectively preventing the droplets from sticking to the substrate. Such hydrophilic surface properties could be obtained by applying proper surfactants such as fetal bovine serum (FBS) [1] for applications where *in vivo* surface treatment is difficult.

2. Modeling ferrofluid droplets on 2D solid substrates

We model the ferrofluid droplets as nearly incompressible fluids using the Smooth Particle Hydrodynamics (SPH) method [2] in order to study and guide the control of their deformation and motion. The governing equation of the droplet body dynamics defined in the domain Ω_f (see **Fig. S2**) is given by

$$\rho(X)\frac{\mathrm{d}v(X)}{\mathrm{d}t} = \nabla \cdot \boldsymbol{\sigma}(X) + \boldsymbol{F}_{\mathbf{body}}(X), \qquad X \in \Omega_f \qquad (S1)$$

where ρ the ferrofluid density, $\boldsymbol{v}$ is the ferrofluid velocity, and $\boldsymbol{F}_{\mathbf{body}}$ is the summation of all the body force per volume applied on the droplet body, given by $\boldsymbol{F}_{\mathbf{body}} = \boldsymbol{F}_{\mathbf{ext}}^{\mathbf{mag}} + \boldsymbol{F}_{\mathbf{ferro}}^{\mathbf{mag}} + \boldsymbol{F}_f + (\rho - \rho_w)\boldsymbol{g} + \boldsymbol{F}_N + \boldsymbol{F}_d + \boldsymbol{F}_S$. $\boldsymbol{F}_{\mathbf{ext}}^{\mathbf{mag}}$ and $\boldsymbol{F}_{\mathbf{ferro}}^{\mathbf{mag}}$ are the external and interactive magnetic force per volume. $\boldsymbol{F}_f$ is the surface friction applied on the droplet boundary surface contacting to the substrate. $(\rho - \rho_w)\boldsymbol{g}$ is the net gravity (water density: ρ_w). $\boldsymbol{F}_N$ is the supporting force from the solid substrate. $\boldsymbol{F}_d$ is the fluid drag applied on the droplet body, which is assumed to be proportional to the material velocity. $\boldsymbol{F}_S$ denotes the continuum surface tension force only defined on the boundary layer Ω_s, which will be discussed in detail later.

To calculate the Cauchy stress $\boldsymbol{\sigma}$, we use the constitutive law of nearly incompressible fluids [3], which is given by

$$\boldsymbol{\sigma} = -p\mathbf{I}, \; p = K\left[(\tfrac{\rho}{\rho_0})^\lambda - 1\right], \qquad (S2)$$

where p is the hydrostatic pressure, K is the bulk modulus, ρ is the fluid density and ρ_0 is the initial fluid density. λ is chosen to be 7 for nearly incompressible fluids. It should be noted that the Van der Waals force between magnetic nanoparticles were included in the nearly incompressible fluid model.

The magnetic force per volume $\boldsymbol{F}_{\mathbf{ext}}^{\mathbf{mag}}$ applied on the FDR at a position $\boldsymbol{r}$ is given by

$$\boldsymbol{F}_{\text{ext}}^{\text{mag}}(\boldsymbol{r}) = -\nabla U_{\text{ext}}(\boldsymbol{r}) = -\nabla(\boldsymbol{M} \cdot \boldsymbol{B}_{\text{ext}}(\boldsymbol{r})), \tag{S3}$$

where $\boldsymbol{M} = \frac{\chi}{\mu_m}\boldsymbol{B}_{\text{ext}}$ is the simplified magnetization of the droplet and μ_m is the magnetic permeability of the ferrofluid droplet. $\boldsymbol{B}_{\text{ext}}$ is modeled using the Biot-Savart law for electromagnets and the magnetic dipole model by discretization for permanent magnets.

To model the surface tension, we use the Continuum Surface Force (CSF model) [4], which approximates the surface tension as a volume force applied on the interface layer Ω_s of two immiscible fluids. For ease of tracking different domains, a color function is defined to mark the domains of the fluids and their interface layer, which is given by,

$$c(x) = \begin{cases} c_1, & X \in \Omega_f \\ c_2, & X \in \Omega_w \\ \frac{(c_1+c_2)}{2}, & X \in \Omega_s \end{cases}. \tag{S4}$$

The surface tension force in the CSF model is given by the Young–Laplace equation as:

$$\boldsymbol{F}_S = (\gamma\kappa\hat{n})\delta_s, \tag{S5}$$

where γ is the coefficient of surface tension, $\kappa = -\nabla \cdot \hat{n}$ is the curvature of the interface boundary layer of the droplet, and $\hat{n} = \frac{\vec{n}}{|\vec{n}|}$ is the unit surface normal vector of the interface layer. δ_s is the surface Dirac delta function with a peak value on the interface boundary layer, so that it constrains the surface tension force to only apply on the interface boundary layer.

Based on the model given by Eqns. (S1) to (S5), we further use a Material Point Method (MPM) to numerically simulate the behaviors of an FDR under an external magnetic field (see **Supplementary Text Section 7**). During the numerical simulations, we made several assumptions to simplify our computation, as our objective here is to provide a guideline for designing and controlling the shape and motion of ferrofluid droplets. We only numerically simulated the 2D dynamics of the droplet in the *x-y* plane, although the model in Eqn. (S1) is general for both 2D and 3D scenarios. In addition, we neglected the interactive magnetic force $\boldsymbol{F}_{\text{ferro}}^{\text{mag}}$ within a droplet to reduce the computation time, assuming that it was much smaller than $\boldsymbol{F}_{\text{ext}}^{\text{mag}}$ when the external magnetic field was relatively small to not induce spikes in the simulated scenarios. The key parameters used in the numerical simulation are summarized in **Table S2**.

3. Estimation of the maximal manipulation force by an FDR

We estimate the maximal pushing force applied on the manipulated objects by an FDR, via a quasi-static force analysis of the objects being manipulated. A hydrogel ball in water subjects to a pushing force F_t by the FDR, a fluid drag force F_d by the surrounding liquid, and a friction force F_f from the bottom surface of the container. Assuming the hydrogel ball is moving at a constant speed, we have $F_t = F_d + F_f$. Here, F_d can be estimated by the Kahn-Richardson fluidic drag model [5], given by.

$$F_d = \pi R^2 \rho_w v^2 (1.84 Re^{-0.31} + 0.293 Re^{0.061})^{3.45}, \tag{S6}$$

where ρ_w is the fluid density and Re is the Reynolds number. v and R are the velocity and radius of the hydrogel ball, respectively. In addition, the friction force F_f is given by,

$$F_f = \frac{4}{3}\pi R^3 (\rho_h - \rho_w) g \mu_h, \tag{S7}$$

where $\rho_h = 1.2$ g·cm^{-3} is the density of the hydrogel ball, g is the acceleration of gravity, and μ_h = ~0.12 is the estimated friction coefficient between the hydrogel ball and the substrate.

By using FDRs with different viscosities and magnetization, the maximum speed of a hydrogel ball before the FDR breaks could be adjusted. As shown in **Fig. S10,** the maximum speed of the hydrogel ball is between 28 mm·s^{-1} and 45 mm·s^{-1} in the experiments when varying the mixing ratio of two ferrofluids. Therefore, the maximal pushing force on the hydrogel ball F_t is estimated to be between 57 μN to 88 μN.

4. Preparation of the objects to be manipulated

As shown in **Fig. S16,** the polypodium acrylate hydrogel was synthesized by the free radical polymerization method [6]. In a typical experiment, 400 mg of sodium acrylate, 35 mg of *N,N′*-methylenebisacrylamide (MBA), and 10 mg of $K_2S_2O_8$ were dissolved in 3 mL of deionized water and ultrasonicated for 30 min. Then, 15 μL of $C_6H_{16}N_4$ was added into the solution to initiate the polymerization reaction. After that, the incompletely polymerized solution was quickly transferred to a tube with a spherical bottom and liquid paraffin contained for further shaping. After 10 h of polymerization at room temperature, hydrogel balls with various sizes were finally obtained.

5. X-ray imaging of FDRs with embedded liquid cargos

The X-ray images of a ferrofluid droplet with a water-based liquid cargo inside were acquired using a Cabinet X-ray system (XPERT 80, Tubtec Scientific). A ferrofluid droplet (MFR-DP1, Supermagnet.de) was prepared in a glass petri dish filled with water. First, X-ray images of the ferrofluid droplet without water-based liquid cargos were taken inside the Cabinet X-ray system. Then, water-based cargos were sequentially injected into the ferrofluid droplet, and the X-ray images were taken at the same condition for comparison.

6. Simulations and calculations

The splitting and merging behaviors of an FDR and its motion in free spaces were performed in Labview 2018 (National Instruments) and Matlab 2020a (Mathworks, Inc.). The distributed magnetic fields from electromagnets and permanent magnets were performed in Matlab 2020a.

7. Numerical simulation of FDRs

We use a hybrid Lagrangian/Eulerian numerical simulation method, Material Point Method (MPM) [7], to numerically simulate the dynamic behavior of an FDR, as MPM allows efficient simulation of materials undergoing extreme deformations. We here briefly explain the procedure of carrying out the MPM algorithm as illustrated in **Fig. S17**. First, the physical quantities of the material points are mapped to the grids using an interpolation algorithm. Then, the physical quantities

associated with the grids are updated on the grids based on the governing equation. Finally, the interpolated physical quantities on the grid are mapped back to these material points. We summarize the key steps in the MPM algorithm as below.

a) **Initialization.** The initial discretization is carried out for P particles (material points), of which the p-th particle has a mass m_p, position $\boldsymbol{X}_p^n$, velocity $\boldsymbol{v}_p^n$, volume V_p^n, deformation gradient tensor $\boldsymbol{F}_p^n$, magnetic moment $\boldsymbol{m}_{mp}^n$, affine velocity matrix $\boldsymbol{C}_p^n$ [8], and other material parameters. Here, the superscript n indicates the time step $t = n\Delta t$.

b) **Mapping from particles to grids**. The Affine Particle-In-Cell (APIC) method [8, 9] is then used to transfer the mass and momentum from the p-th particle ($p = 1, ..., P$) to the i-th grid ($i = 1, ..., M$), as given by,

$$m_i^n = \sum_p w_{ip}^n m_p, \tag{S8}$$

$$m_i^n \boldsymbol{v}_i^n = \sum_p w_{ip}^n m_p \left[\boldsymbol{v}_p^n + \boldsymbol{C}_p^n (\boldsymbol{X}_i - \boldsymbol{X}_p^n)\right], \tag{S9}$$

where $w_{ip}^n = \mathcal{N}(\boldsymbol{X}_p^n - \boldsymbol{X}_i)$ is the interpolation weight from the p-th particle to the i-th grid at the time step $t = n\Delta t$, and $\mathcal{N}(\boldsymbol{X})$ is chosen to be the quadratic B-spline interpolation kernel. $\boldsymbol{X}_i$ denotes the regular Cartesian grid node position.

c) **Updating grids**. The force $\boldsymbol{f}_i^n$ and velocity $\boldsymbol{v}_i^n$ on the i-th grid at the time step $t = n\Delta t$ are calculated using a formulation similar to that in [10] given by,

$$\boldsymbol{f}_i^n = -\sum_p V_p^n \boldsymbol{\sigma}_p^n \nabla w_{ip}^n + \sum_p w_{ip}^n \boldsymbol{f}_p^n, \tag{S10}$$

$$\boldsymbol{v}_i^{n+1} = \boldsymbol{v}_i^n + \Delta t \boldsymbol{f}_i^n / m_i, \tag{S11}$$

where $\boldsymbol{\sigma}_p^n$ is the Cauchy stress, and $\boldsymbol{f}_p^n$ represents the body forces, which have been introduced in **Supplementary Text Section 2**.

d) **Mapping from grids to particles**. We use APIC to map the grid information back to the particles and update the affine velocity matrix $\boldsymbol{C}_p$ and the velocity $\boldsymbol{v}_p$ of the material point, given by

$$\boldsymbol{C}_p^{n+1} = \frac{4}{\Delta X^2} \sum_i w_{ip}^n \boldsymbol{v}_i^n (\boldsymbol{X}_i - \boldsymbol{X}_p^n)^T, \tag{S12}$$

$$\boldsymbol{v}_p^{n+1} = \sum_i w_{ip}^n \boldsymbol{v}_i^n, \tag{S13}$$

where ΔX is the grid spacing.

e) **Updating particles.** The deformation gradient tensor and the position of the material point are updated according to,

$$\boldsymbol{F}_p^{n+1} = \left(\boldsymbol{I} + \Delta t \boldsymbol{C}_p^{n+1}\right) \boldsymbol{F}_p^n, \tag{S14}$$

$$\boldsymbol{X}_p^{n+1} = \boldsymbol{X}_p^n + \Delta t \boldsymbol{v}_p^{n+1}, \tag{S15}$$

where $\boldsymbol{I}$ is an identity matrix.

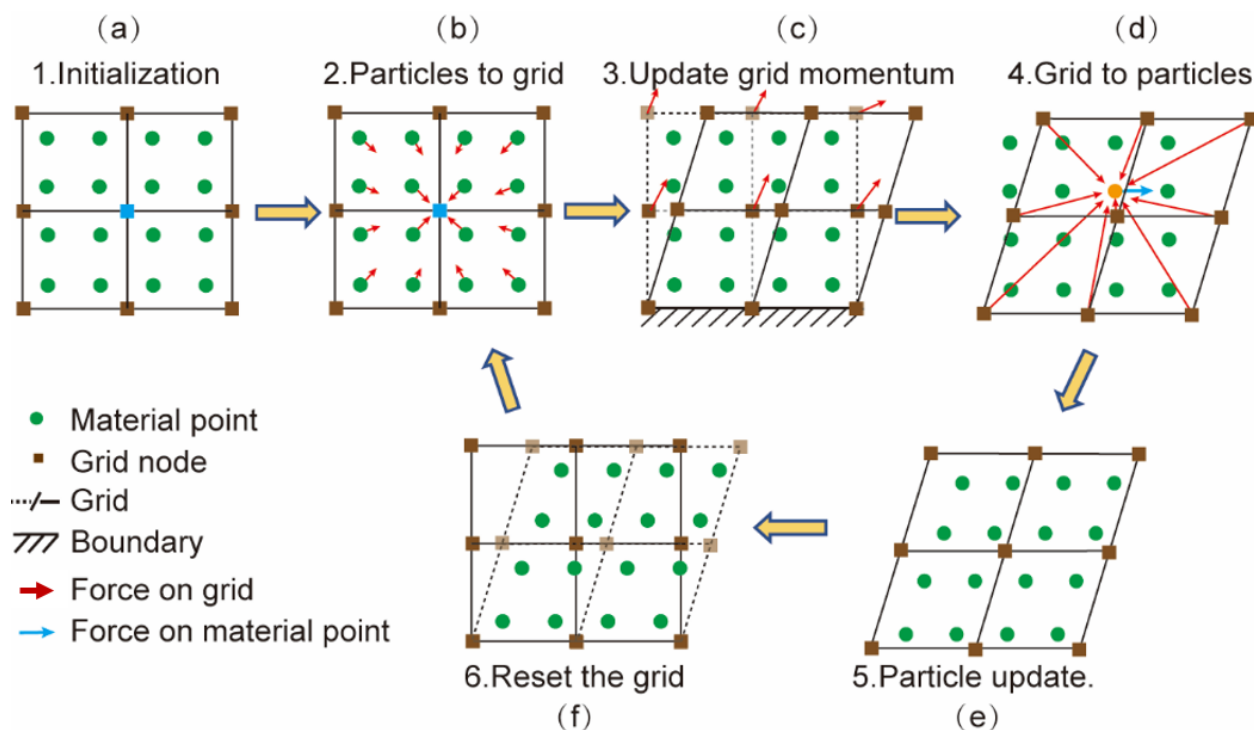f) **Iteration.** Return to b) for the next time step.

Fig. S17. Schematic diagram of the Material Point Method (MPM). (a) Initial discretization into material points. (b) Mapping information from particles (material points) to the grids. (c) Updating grids. (d) Mapping the grid information back to the particles. (e) Updating particles. (f) Resetting the grid and return to the step (b).

Supplementary Movies

Movie S1. **Mechanism and characterization of controlling large complex shapes of FDRs.**
This video first shows the splitting and merging behaviors of an FDR in a glass petri dish filled with water. It then shows the reconfiguration of a ferrofluid droplet by programming external magnetic fields spatiotemporally using permanent magnets.

Movie S2. **Mechanism and characterization of controlling motions of FDRs.**
This video first shows the external magnetic field and potential energy distribution for controlling the locomotion of an FDR. It then shows the locomotion of an FDR driven in the single-coil and double-coil modes. The locomotion of an FDR in normal saline, phosphate-buffered saline and glycerol-water mixture in different viscosities is also presented. Finally, it shows the coordinated motions of multiple FDRs.

Movie S3. **Mechanism and characterization of FDRs navigating in confined spaces.**
This video shows experimental results of navigating through tubes in various diameters by an FDR driven in the double-coil and single-coil modes. It then shows that an FDR navigates through a meandering channel and a complex maze with narrow gaps.

Movie S4. Efficient manipulation of delicate objects by shape-programmable FDRs.
This video first shows that an ellipse-shaped FDR sorted delicate objects in a clustered environment. It then shows that a ring-shaped FDR trapped, transported and released multiple delicate objects simultaneously.

Movie S5. Cargo delivery in tubal environments towards biomedical applications.
This video shows the procedure of loading, carrying and releasing liquid cargos by an FDR as a liquid capsule. It then shows that the liquid capsule navigated through a vascular phantom to deliver the liquid cargo on-demand. The same liquid capsule is shown to navigate through a complex maze while carrying the liquid cargo without breaking.

Movie S6. Multiple FDRs demonstrating programmable fluidic mixing by coordinated independent motion control.
This video first shows an FDR disassembled into multiple sub-FDRs and then worked as pistons and valves for fluidic mixing functions. It then shows addressable mixing and sequential mixing of multiple dyes by coordinating the motions of these sub-FDRs.

SI References

1. Carrondo, M.J., Griffiths, B., Moreira, J.L. (eds.), Animal cell technology: from vaccines to genetic medicine. *Springer Science & Business Media.* 399 (2012).
2. Monaghan J.J., Simulating free surface flows with SPH. *J. Comput. Phys.*, **110**(2), 399-406 (1994).
3. Becker, M., Teschner, M., Weakly compressible SPH for free surface flows. *Proceedings of the 2007 ACM SIGGRAPH/Eurographics Symposium on Computer Animation. Eurographics Association*, 209-217 (2007).
4. Brackbill, J., U., Douglas B., K, Charles Z., A continuum method for modeling surface tension. *J. Comput. Phys.*, **100**(2), 335-354 (1992).
5. Floyd, S., Pawashe, C., Sitti, M., Two-dimensional contact and noncontact micromanipulation in liquid using an untethered mobile magnetic microrobot, *IEEE Tran. Robot.*, **25**(6), 1332-1342 (2009).
6. Wang, X., Li, M., Wang, D., Zhang, H., Duan, D., Zang, D., Song, B., Dong, B., Low-cost, robust pressure-responsive smart windows with dynamic switchable transmittance, *ACS Appl. Mater. Inter.*, **12**(13), 15695-15702 (2020).
7. Gaume, J., *et al.* Dynamic anticrack propagation in snow. *Nat. Commn.*, **9**(1), 1-10 (2018).
8. Jiang, C., Schroeder, C., Selle, A., Teran, J., Stomakhin, A., The affine particle-in-cell method. *ACM Transactions on Graphics (TOG)*, **34**(4), 1-10 (2015).
9. Hu, Y., *et al.,* A moving least squares material point method with displacement discontinuity and two-way rigid body coupling. *ACM Transactions on Graphics (TOG)*, **37**(4), 1-14 (2018).
10. Gao, M., Tampubolon, A.P., Jiang, C., Sifakis, E., An adaptive generalized interpolation material point method for simulating elastoplastic materials. *ACM Transactions on Graphics (TOG)*, **36**(6), 1-12 (2017).